Russian Journal of Earth Sciences Online ISSN: 1681-1208

Special Issue: "Kamchatka Earthquake M 8.8 on July 29, 2025"

Source Parameters of Strong Kamchatka Earthquakes in 2025 ($M_W > 7.0$) from Surface Wave Data

A. I. Filippova[*,1,2] **and A. S. Fomochkina**[2,3]

[1]Pushkov Institute of Terrestrial Magnetism, Ionosphere and Radio Wave Propagation of RAS, Moscow, Troitsk, Russian Federation
[2]Institute of Earthquake Prediction Theory and Mathematical Geophysics of RAS, Moscow, Russian Federation
[3]University of Oil and Gas "Gubkin University", Moscow, Russian Federation
* **Correspondence to:** Alena Filippova, aleirk@mail.ru

Abstract: We consider four strong earthquakes with $M_W > 7.0$ that occurred in 2025 near the Kamchatka Peninsula: the foreshock on July 20, mainshock on July 29, and two aftershocks on September 13 and 18. Their source parameters are estimated from teleseismic surface wave records in instant point and finite-fault (elliptical dislocation with a finite duration) source approximations. In addition, rupture planes are identified based on seismological data. The obtained rupture lengths of the study seismic events are discussed in detail as they are characterized by good resolution. They are compared to USGS finite-fault models, distributions of aftershocks, and some existing scaling relations between subsurface rupture length and magnitude. The July 29, 2025 mainshock is also compared to the November 4, 1952 earthquake with $M_W = 8.8$–9.0. Two scaling relations, providing the best fitting for earthquakes with $M_W \geq 8.0$, are selected based on the obtained results and USGS data.

Keywords: Seismic moment tensor, finite-fault modeling, rupture length, surface waves, Kamchatka megathrust earthquake

Citation: Filippova A. I. and Fomochkina A. S. (2026), Source Parameters of Strong Kamchatka Earthquakes in 2025 ($M_W > 7.0$) from Surface Wave Data, *Russian Journal of Earth Sciences*, 26, ES2012, EDN: ZDOCIT, https://doi.org/10.2205/2026es001122

Research Article

Received: February 2, 2026
Accepted: May 25, 2026
Published: July 1, 2026

1. Introduction

A strong earthquake ($M_W = 8.8$) struck the Kamchatka Peninsula on July 29, 2025 at 23:24 UTC (Figure 1a), was felt over a vast area, caused material damage, and induced a tsunami influencing the eastern shore of the peninsula (https://earthquake.usgs.gov/earthquakes/eventpage/us6000qw60/executive). It was preceded by a foreshock series with the strongest event recorded on July 20 at 6:49 ($M_W = 7.4$) and followed by thousands of aftershocks with the strongest ones recorded on September 13 and 18 (2:37, $M_W = 7.4$ and 18:58, $M_W = 7.8$, respectively) (https://earthquake.usgs.gov). As with all the strong seismic events, the Kamchatka earthquake raises numerous scientific questions. Its rupture (or fault) length is of particular interest in the context of the existing scaling relations, connecting subsurface rupture length and magnitude [e.g., *Wells and Coppersmith*, 1994; *Zavyalov and Zotov*, 2021], as all of them are naturally constructed based on limited data about events with $M_W \geq 8.0$.

The study region is characterized by a unique tectonic position as there is a junction zone where, according to some researchers, the Pacific Plate borders the Okhotsk and North American plates (Figure 1a) [*Bird*, 2003] or, according to others, the Pacific Plate borders the Bering Sea and North American plates [*Kogan et al.*, 2017]. The northeasternmost part of the Pacific Plate is subducting northwestward along the Kuril-Kamchatka trench with a rate of about 8 cm/year [*DeMets et al.*, 1990]. This makes the Kamchatka Peninsula one of the largest volcanic arcs in the world [e.g., *Nishizawa et al.*, 2017] and determines its high seismic potential. Tens of earthquakes with $M \geq 7.0$, including the strongest November 4,

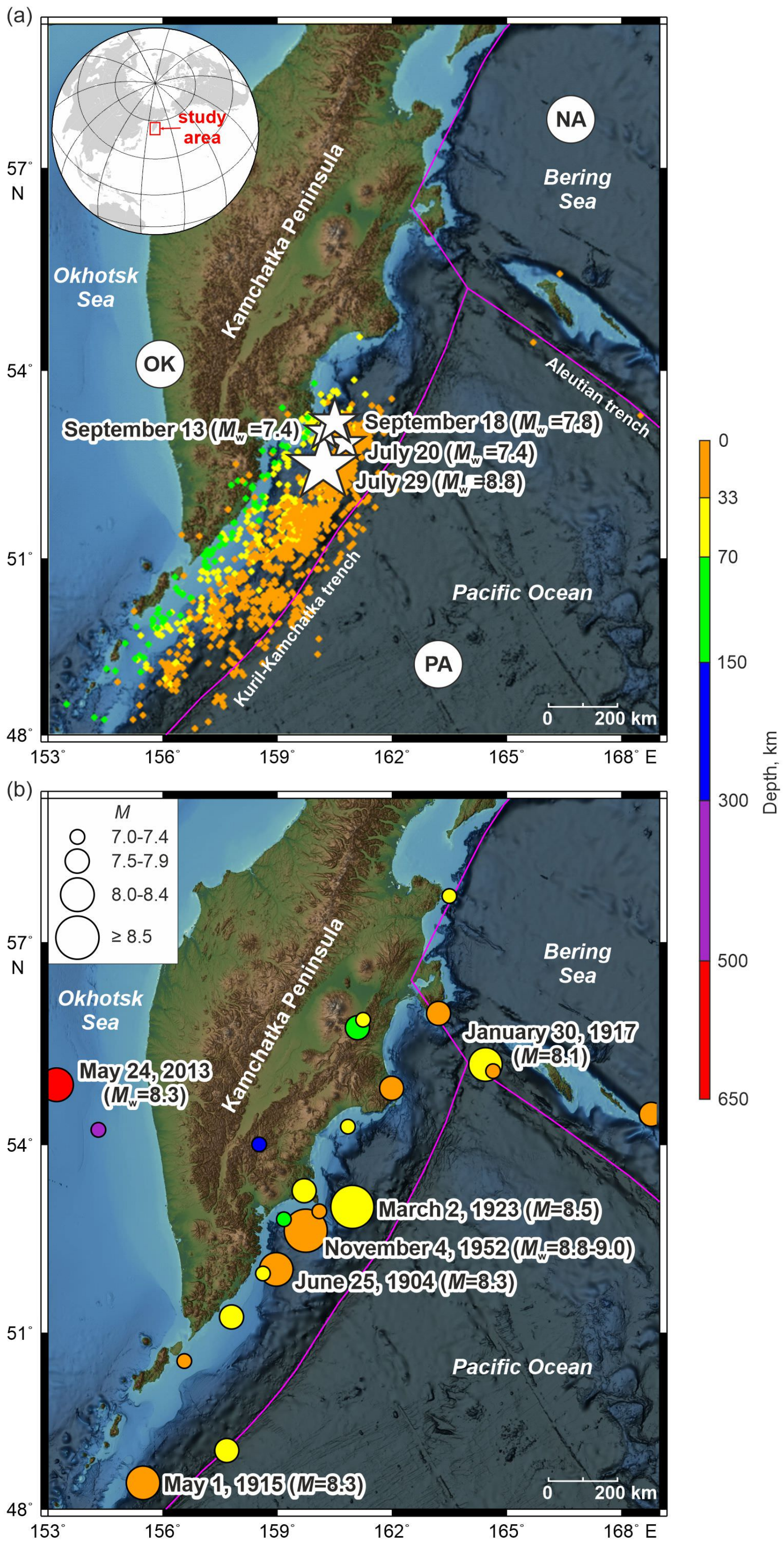

Figure 1. Study earthquakes (stars) and epicenters of seismic events with $M \geq 4.5$ which occurred from July 20, 2025 to October 1, 2025 (https://earthquake.usgs.gov) (a). Epicenters of earthquakes with $M \geq 7.0$ (1950–2024) (https://earthquake.usgs.gov) and the strongest early instrumental seismic events ($M \geq 8.0$, 1900–1950) [*Ruppert et al.*, 2007] in the study region (b). Magenta lines are lithospheric plate boundaries according to [*Bird*, 2003]. Letters in circles are lithospheric plates: NA – North American, OK – Okhotsk, PA – Pacific. The region position is mapped in the inset in panel (a). In panel (b), dates and magnitudes are indicated only for earthquakes with $M \geq 8.0$.

1952 earthquake with $M_W = 8.8$–9.0 [*Johnson and Satake*, 1999; *Kanamori*, 1976], occurred in this region during the last 75 years and several early instrumental events with $M \geq 8.0$ [*Ruppert et al.*, 2007] are known here (Figure 1b).

In this study, we determine source parameters of the mainshock, its strongest foreshock and two strongest aftershocks from teleseismic surface wave records. The earthquakes are modeled both in instant point and finite-fault source (as an elliptical dislocation with a finite duration) approximations, as well as real rupture planes are selected based only on seismological data. The obtained results on rupture lengths are compared with currently available finite-fault models constructed in USGS (https://earthquake.usgs.gov) and published in [*Xu et al.*, 2025], source parameters of the November 4, 1952 Kamchatka earthquake [*Johnson and Satake*, 1999; *Kanamori*, 1976] and analyzed in the context of some existing scaling relations [*Leonard*, 2010; *Thingbaijam et al.*, 2017; *Wells and Coppersmith*, 1994; *Zavyalov and Zotov*, 2021].

2. Data and Methods

Calculation of source parameters consists of three stages: (i) data selection and processing, (ii) modeling an earthquake in an instant point source approximation, and (iii) modeling an earthquake source as a shear elliptical dislocation with a finite duration (finite-fault approximation). At the first stage, we collect waveforms of the considered seismic events recorded at broadband remote (with epicentral distances $\Delta > 20°$) seismic stations of the GSN network and select those of them which are characterized by a high signal-to-noise ratio. Finally, records from about 20 seismic stations, located in different azimuths from the epicenters of the study earthquakes, are chosen (Figure 2). Frequency-time analysis, which is an analogue of a multiple narrow-band filtration, is applied to isolate the fundamental mode of Rayleigh and Love waves and to determine their amplitude spectra [*Keilis-Borok*, 1989]. Information about a number of the used seismic stations, their epicentral distances, and period ranges, in which surface wave spectra are obtained, is summarized in Table 1.

Table 1. Parameters of the initial data

Earthquake	Number of stations	Epicentral distance, °		Period range, s	
		minimum	maximum	full	shorten
July 20	23	33.72	82.03	60–320	60–100
July 29	21	29.40	118.89	160–340	160–240
September 13	19	33.83	111.43	70–320	70–150
September 18	20	40.57	118.93	70–320	70–150

At the second stage, the determined amplitude spectra in the full period ranges, indicated in Table 1, are inverted to earthquake source parameters in an instant point source approximation using a method proposed by B. G. Bukchin [*Bukchin*, 1990]. According to the applied approach, a pure double-couple source is considered. In such an approximation, a seismic moment tensor can be described by a scalar seismic moment and angles, characterizing two equivalent nodal planes (or angles determining principal stress axes). In addition to these parameters, a centroid depth is estimated. A moment magnitude is calculated from the scalar seismic moment [*Hanks and Kanamori*, 1979]. In the inversion procedure, we minimize values of the normalized residual function, characterizing the deviation between synthetic amplitude spectra and spectra obtained with the frequency-time analysis (referred to as observed spectra hereafter). A grid search is applied in the software realizing the used method [*Bukchin et al.*, 2005]. Full possible ranges of the estimated parameters are explored.

Due to the symmetry of surface wave amplitude spectra, there are four equivalent focal mechanism solutions varying in vertical axes and slip directions [*Mendiguren*, 1977]. To overcome this uncertainty, P-wave first-motion polarities can be used as additional information to constrain a unique solution [*Lasserre et al.*, 2001]. It is worth noting, that

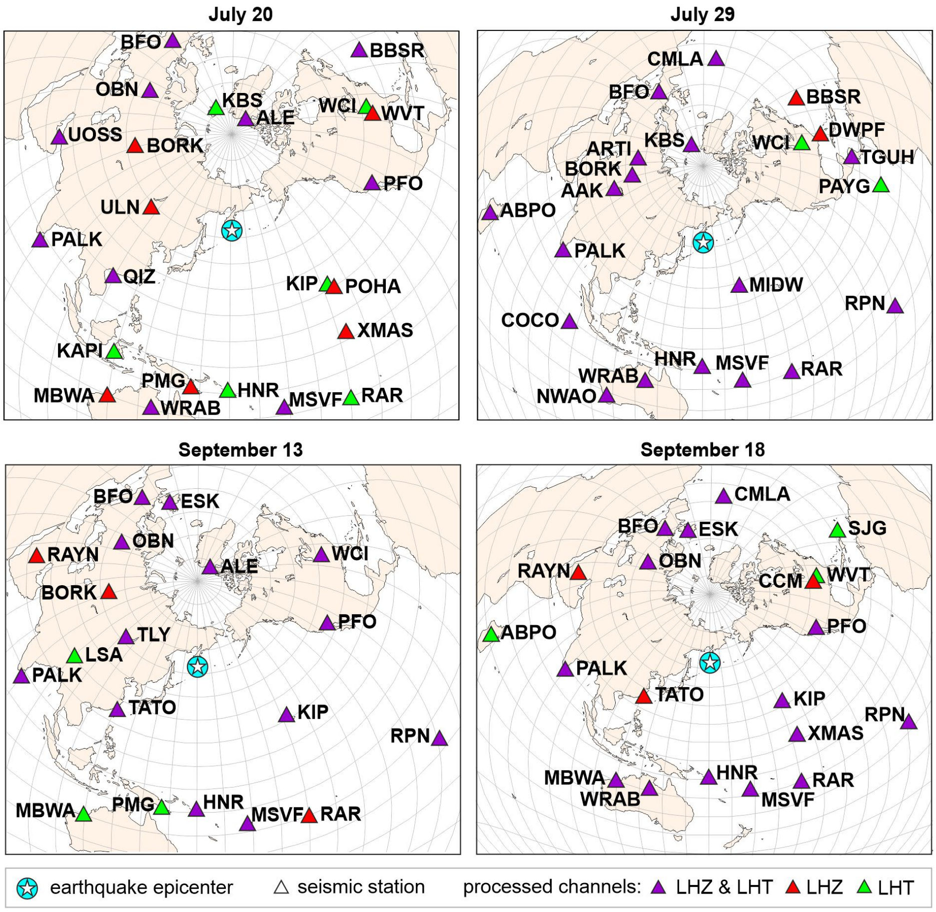

Figure 2. Epicenters of the study earthquakes and seismic stations, whose records are used in the inversion of source parameters. LHZ is a vertical component of the record, LHT is a transversal component computed from the LHN (northern) and LHE (eastern) components.

their number and azimuthal distribution can be not enough to determine a focal mechanism from only this kind of data. In our study, we apply P-wave first-motion polarities recorded at teleseismic stations and reported in the ISC-bulletin (https://isc.ac.uk).

To describe the crustal structure in the source areas of the considered earthquakes, the 3D global crustal model 3SMAC is used [*Nataf and Ricard*, 1996]. It should be emphasized that changes in the crustal model do not significantly affect the obtained results (for example, see [*Seredkina et al.*, 2020]). For the upper mantle structure, the 1D spherical symmetric PREM model [*Dziewonski and Anderson*, 1981] is applied. Surface wave attenuation is estimated for the same model.

At the final stage, we model an earthquake source as a shear elliptical dislocation with a finite duration (finite-fault source) following [*Bukchin*, 1995]. As at the previous stage, a grid search with minimizing the misfits between synthetic and observed spectra is applied. The inversion is performed in shorten period ranges in comparison with those used in an instant point source approximation (Table 1). The following integral parameters, characterizing source dimensions and faulting development, are calculated: lengths of the source ellipse major and minor axes ($l_{\max}$ and $l_{\min}$), duration (Δt), modulus of an average value of an instant centroid velocity ($|v|$), an angle between the fault strike axis and major axis of the source ellipse (φ_l), and an angle between the fault strike axis and the instant centroid velocity axis (φ_v). According to [*Bukchin et al.*, 2020], real source dimensions (L – rupture length) and duration (T) are related to the integral characteristics in the following manner: $L = 3 \cdot l_{\max}$, and $T = 2.5 \cdot \Delta t$.

An interesting aspect of the applied method is that it potentially allows us to select a real rupture (or fault) plane from equivalent nodal planes of a focal mechanism. For this purpose, integral source parameters are calculated for both the nodal planes and a rupture plane is characterized by lower values of the normalized residual function [*Bukchin*, 2017]. The best-pronounced difference in residuals is traced for earthquakes with a significant strike-slip component in their sources. Nevertheless, judging from independent geophysical and geological information, even a small difference, observed for almost pure thrusts and normal faults, reliably indicates a real fault plane [*Bukchin et al.*, 2020; *Filippova et al.*, 2025; *Filippova et al.*, 2022, 2024]. Therefore, we perform such an analysis in this study.

3. Results and Discussion

3.1. Instant Point Source

The results, obtained for four study earthquakes in an instant point source approximation, and normalized residual functions (ε), characterizing them, are shown in Figure 3. We compare them with parameters reported in main seismological agencies and currently available papers (Table 2). First, it should be noted that our moment magnitudes (and scalar seismic moments, respectively) are generally slightly lower than other estimates. Nevertheless, the difference is not large. For M_W, it is mostly 0.1 and in some cases can reach 0.2. For the July 29, 2025 earthquake, our M_W equals to estimates by GCMT and [*Xu et al.*, 2025]. The observed discrepancies are predominantly resulted from difference in frequency ranges of the initial data. From our point of view, this is the most significant factor for the mainshock for which very long-period W-phase records (200–1000 s) are used in USGS [*Hayes et al.*, 2009]. The same reason can explain high scattering in source depths which can be as high as about 20 km according to different agencies, [*Xu et al.*, 2025], and our study (Table 2, Figure 3). The September 13, 2025 earthquake is an exception as its depth values, including ours, are relatively close to each other – their variations are in a 10-km range.

Table 2. Instant point source parameters of the study earthquakes according to main seismological agencies and currently available papers

Earthquake	Reference	$M_0 \cdot 10^{20}$, N·m	M_W	*h*, km	Nodal Plane			Φ, °
					Strike, °	Dip, °	Slip, °	
July 20	GCMT	2.28	7.5	26.9	219	12	88	17
	USGS$^{W\text{-}phase}$	1.37	7.4	23.5	217	24	84	12
	USGS$^{centroid\ mt}$	1.44	7.4	34.8	224	25	96	19
	USGS^{mt}	1.04	7.3	47	221	17	94	19
	GEOFON	1.6	7.4	20	228	15	102	21
July 29	GCMT	145	8.7	36.9	214	19	87	5
	USGS$^{W\text{-}phase}$	222	8.8	21.5	198	18	51	13
	GEOFON	190	8.8	20	209	13	73	7
	[*Xu et al.*, 2025]	118*	8.7*	40	212.6	19.8	81.2	6
September 13	GCMT	1.34	7.4	44.2	211	24	86	6
	USGS$^{W\text{-}phase}$	1.43	7.4	40.5	215	23	89	7
	USGS$^{centroid\ mt}$	1.22	7.3	47.1	210	32	90	5
	GEOFON	1.2	7.3	40	211	21	82	10
September 18	GCMT	7.91	7.9	24.9	211	15	82	11
	USGS$^{W\text{-}phase}$	6.87	7.8	19.5	212	18	84	8
	USGS$^{centroid\ mt}$	6.14	7.8	36	216	25	92	1
	GEOFON	6.1	7.8	33	214	15	89	10

Notes: GCMT (https://www.globalcmt.org), USGS (https://earthquake.usgs.gov), GEOFON (https://www.gfz-potsdam.de). Superscripts in USGS indicate a type of data used and a procedure for their inversion: *W-phase* marks the W-phase inversion [*Hayes et al.*, 2009; *Kanamori and Rivera*, 2008] and this is the most preferred solution by USGS, *centroid mt* is based on long-period body and surface waves [*Dziewonski and Woodhouse*, 1983], *body-wave mt* is based on long-period body waves [*Sipkin*, 1982]. An asterisk marks parameters obtained in a finite-fault source approximation.

In spite of differences in frequency ranges of the initial data, discussed above, various determinations of focal mechanisms are very close to each other. To demonstrate this quantitatively, we calculate a Kagan-angle (Φ) [*Kagan*, 1991, 2007] between our solutions (Figure 3) and the best double-couples reported in Table 2. This is an angle in a 3D space to which one double-couple should be rotated to coincide with other one. For identical double-couples, Φ is 0° and its maximum value is 120° for totally different focal mechanisms. In our case, Φ-values are in the range of 1–21° (Table 2) that indicates proximity of the compared solutions. It is worth noting that such a consistency evidences for high percentage of double-couple component in the sources of the study seismic events. This is in agreement with statistical analysis results [*Rösler and Stein*, 2022; *Zaccagnino and Doglioni*, 2022] showing that subduction thrust earthquakes are characterized by decreased non-double-couple component relative to strike-slips and normal faults due to larger and more uniform active tectonic settings.

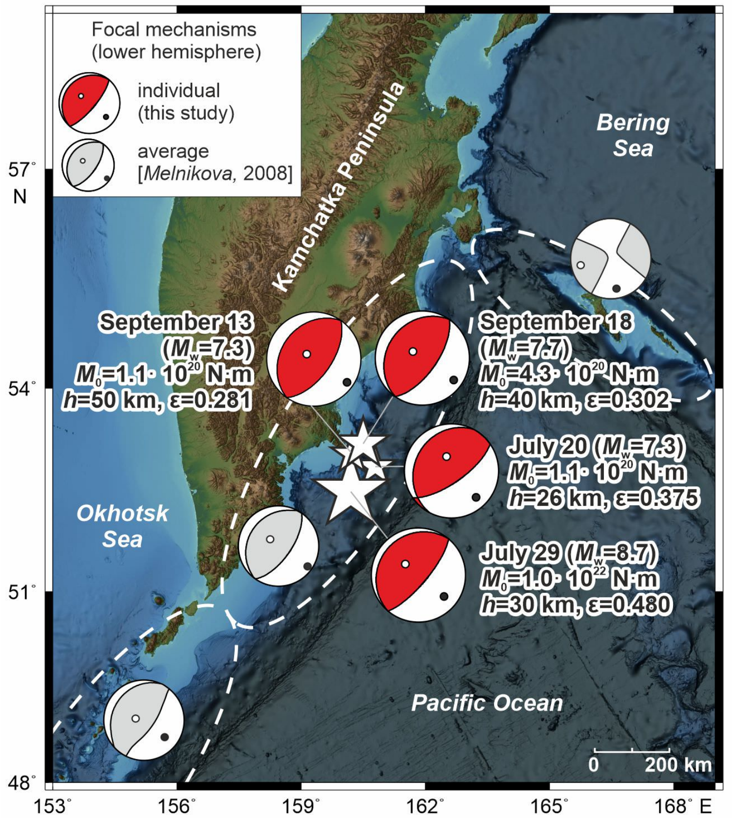

Figure 3. Results obtained for four study earthquakes in an instant point source approximation with normalized residual functions (ε) characterizing them. White dashed ellipses schematically contour areas in which average focal mechanisms are estimated in [*Melnikova*, 2008].

The focal mechanisms, obtained for all the study earthquakes, are very similar to each other – they are pure or almost pure thrusts formed under the influence of the near horizontal SE-NW compression that agrees well with the direction of the Pacific Plate subduction [*DeMets et al.*, 1990]. They are close to an average focal mechanism, determined for this segment of the Kuril-Kamchatka trench by [*Melnikova*, 2008] (Figure 3), and reflect a regional strain field according to the latest release of the World Stress Map [*Heidbach et al.*, 2016].

3.2. Finite-Fault Source

As we have mentioned above, the integral finite-fault parameters of the considered earthquakes are calculated for both the nodal planes determined in an instant point source approximation (Figure 3). An example of the obtained results, illustrating the difference in the normalized residual functions (ε) which allows us to discriminate the rupture plane [*Bukchin*, 2017], is shown in Figure 4. All the estimated ε-values are presented in Table 3 and evidence for the gently-dipping nodal planes (NP_1 with dip angles of 15–30°) to be the rupture planes. This is in agreement with data on geometry of the subduction zone in the study region [*Gorbatov et al.*, 1997; *Hayes et al.*, 2018].

Table 3. Normalized residual functions (ε), calculated in a finite-fault approximation, corresponding to both the nodal planes (NP) of the determined focal mechanisms (Figure 3)

Earthquake	NP_1 (strike°, dip°, slip°)	ε_1	NP_2 (strike°, dip°, slip°)	ε_2
July 20	208, 22, 64	0.360	55, 70, 100	0.375
July 29	220, 15, 90	0.243	40, 75, 90	0.260
September 13	215, 30, 90	0.250	35, 60, 90	0.274
September 18	215, 25, 90	0.268	35, 65, 90	0.284

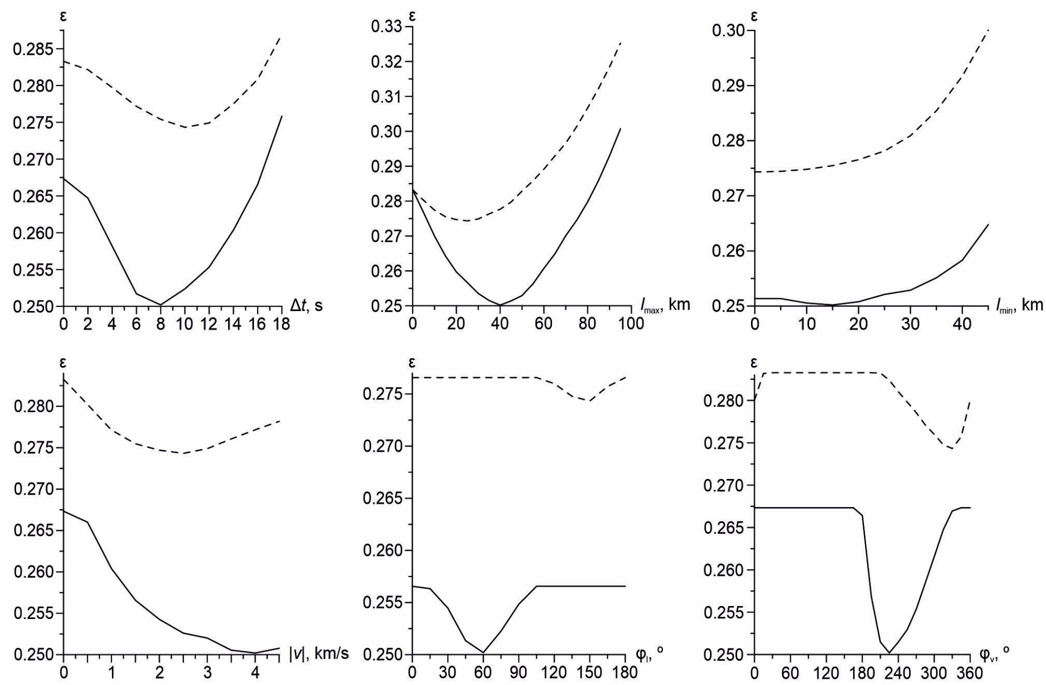

Figure 4. Partial residual functions for the integral source parameters for the September 13, 2025 earthquake. Solid and dashed lines correspond to the parameters calculated for the nodal planes NP_1 and NP_2 in Table 3 with strike angles of 215° and 35°, respectively.

Theoretically, the observed variations in ε-values are related to differences in radiation patterns of surface waves generated by a finite-fault source (Figure 5) which is modeled in our case as an elliptical dislocation with a finite duration. It is worth noting that such a difference is very slight for Love waves and more pronounced for Rayleigh waves propagating perpendicularly to the nodal planes and can be traced for all the considered seismic events due to approximately uniform distribution of the analyzed seismic stations (Figure 2).

The integral parameters of a shear elliptical dislocation, obtained for the determined rupture planes, are listed in Table 4. First, we emphasize that indicated $|v|$-estimates should not be interpreted as rupture velocities as they do not take into account a faulting character (unilateral or bilateral faulting). Second, the resolution of these parameters should be taken in mind in their interpretation. The length of the major axis of the source ellipse (l_{max}) is well-resolved for all the considered events (Table 4). This is illustrated for the September 13, 2025 earthquake as a distinct minimum of the normalized residual function is observed at the obtained value of this parameter (Figure 4). This allows us to discuss in detail the rupture lengths ($L = 3 \cdot l_{max}$ [*Bukchin et al.*, 2020]) of the study earthquakes further. The resolution of the minor axis length and source duration is also generally good except for the aftershocks: l_{min} varies in a range of 10–20 km for the first aftershock (Figure 4) and Δt varies from 8 to 10 s for the second one without significant increase of ε-values. On the contrary, integral velocities and angles, characterizing the source ellipse position and, to some extent, rupture direction, are poorly resolved except the mainshock for which only $|v|$-value is not well-constrained and can vary in a wide range of 2.5–4.0 km/s. As in the case of the rupture plane selection, the resolution of the integral parameters is controlled by surface wave radiation patterns within the analyzed period ranges (shorten period ranges in Table 1). It is quite obvious that the obtained estimates for the July 29, 2025 mainshock are characterized by the best resolution as the difference between instant point and finite-fault radiation patterns are the most pronounced for this event (Figure 5). The problems, arising in integral velocity resolution, are probably related to the complex character of the real rupture velocity which increased from 1.5 to 2.8 km/s during the faulting according to the back-projection analysis [*Xu et al.*, 2025].

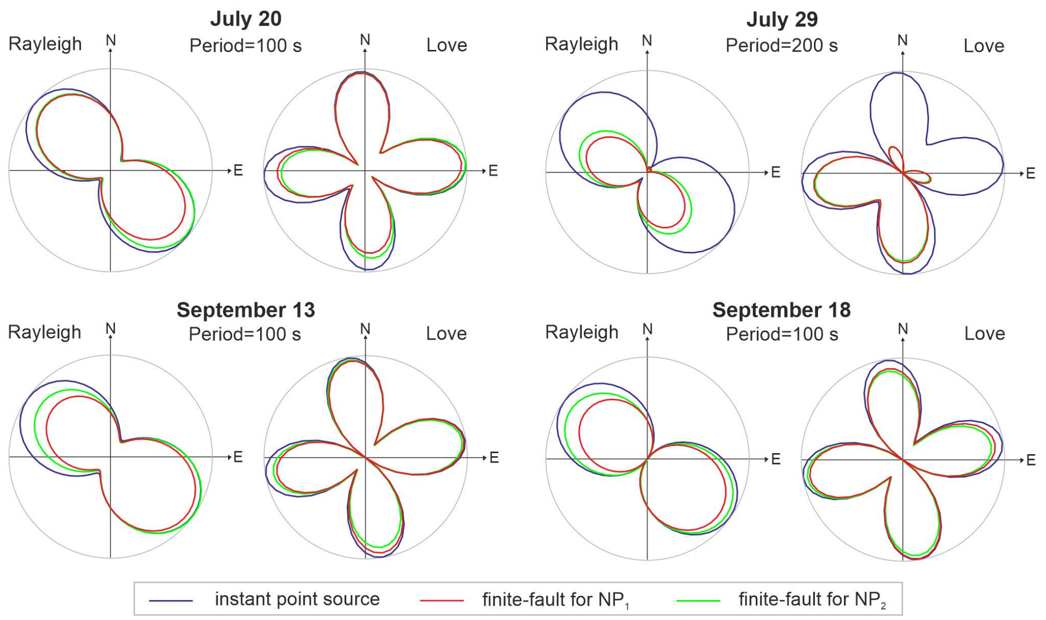

Figure 5. Radiation patterns of Rayleigh and Love waves for instant point and finite-fault sources at the periods approximately corresponding to a half of the period range in which a finite-fault source is modeled (shorten period ranges in Table 1). The radiation patterns in a finite-fault source approximation are calculated for both the nodal planes shown in Figure 3 (notations of nodal planes correspond to Table 3) and the integral source parameters obtained in this study (Table 4).

Table 4. Integral source parameters of the study earthquakes calculated for the determined rupture planes (NP_1 in Table 3)

Earthquake	l_{max}, km	l_{min}, km	Δt, s	$\|v\|$, km/s	φ_l, °	φ_v, °
July 20	45	30	10	4.0*	15*	180*
July 29	200	90	52	3.5*	0	0
September 13	40	15*	8	4.0*	60*	225
September 18	45	25	9*	3.0*	60*	315*

Notes: An asterisk marks parameters with poor resolution. For the July 29, 2025 mainshock, the source depth is recalculated in a finite-fault source approximation and equals to 55 km.

Our estimates of the real rupture lengths and source durations, based on integral source parameters, along with the corresponding source characteristics from finite-fault

USGS models (https://earthquake.usgs.gov) are summarized in Table 5. For the July 29, 2025 mainshock, our rupture length equals to the USGS estimate and is confirmed by a distribution of aftershock epicenters which are grouped within the area with a length of 600 km (Figure 6b). Longer rupture is obtained for this earthquake from analysis of teleseismic P- and SH-waves performed in [*Xu et al.*, 2025] using the same method as those employed in USGS [*Ji et al.*, 2002]. Nevertheless, the USGS finite-fault model (Version 5) is based on a larger number of data (https://earthquake.usgs.gov/earthquakes/eventpage/us6000qw60/finite-fault). Remarkably, the same authors [*Xu et al.*, 2025] reports shorter rupture (∼500 km) based on P-wave back-projection analysis. In contrast to the rupture length, our value of its duration is significantly shorter than all the other estimates (Table 5). This can be due to the fact that relative moment rate is low during the first 40–50 s according to USGS and [*Xu et al.*, 2025] and our model describes only the high-rate part of the rupture.

Table 5. Comparison of the obtained real rupture lengths and source durations with finite-fault models reported in USGS (https://earthquake.usgs.gov) and currently available papers

Earthquake	This study		USGS		[*Xu et al.*, 2025]	
	L, km	*T*, s	*L*, km	*T*, s	*L*, km	*T*, s
July 20	135	25	70	22	–	–
July 29	600	130	600	192	700	200
September 13	120	20	120	28	–	–
September 18	135	22.5*	120	37	–	–

Notes: An asterisk marks parameters with poor resolution. Versions of the USGS finite-fault models correspond to October 20, 2025: Version 1 – the July 20 and September 13 earthquakes, Version 5 – the July 29 earthquake, Version 2 – the September 18 earthquake.

For the July 20, 2025 foreshock, a large difference is seen between our rupture length and the USGS finite-fault model while various source durations are in agreement with each other (Table 5). Most of the aftershocks of this seismic event are concentrated within the area with a length of about 150 km (Figure 6a) that provides evidences for the correctness of our estimate. It is interesting to note that a change in the strike of the rupture plane – from 208° for the major foreshock to 220° for the mainshock – is obviously observed in their aftershock distributions (Figure 6). For the two largest aftershocks, rupture lengths, determined in this study and in USGS, are close to each other instead of difference in their moment magnitudes but our values of rupture duration are slightly shorter in both cases (Table 5).

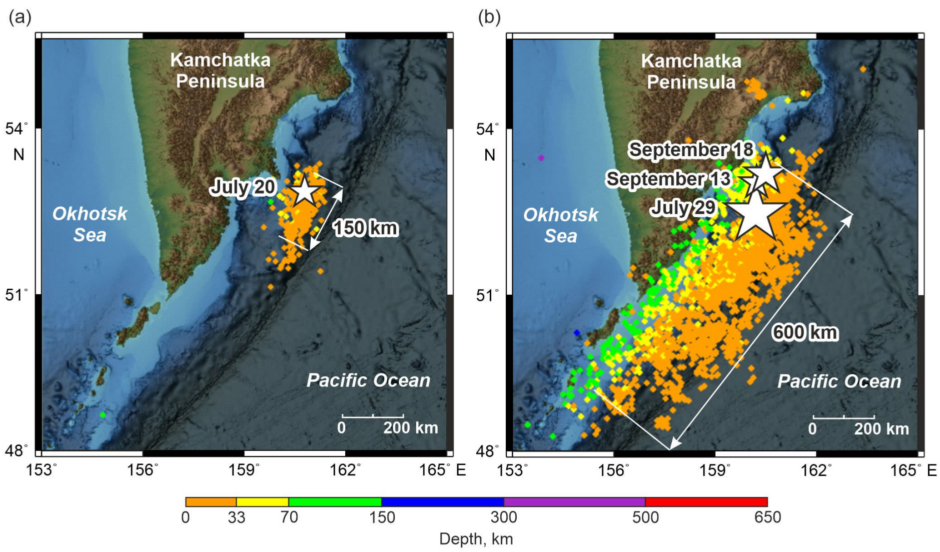

Figure 6. Epicenters of seismic events with $M \geq 2.5$ which occurred from July 20, 2025 to July 28, 2025 (a) and from July 29, 2025 to October 1, 2025 (b) (https://earthquake.usgs.gov).

Finally, we compare the rupture lengths, obtained for the considered seismic events, with other large earthquakes and some existing scaling relations between subsurface rupture length and magnitude [*Leonard*, 2010; *Thingbaijam et al.*, 2017; *Wells and Coppersmith*, 1994; *Zavyalov and Zotov*, 2021]. For the mainshock, which is of the main interest as all the discussed relations are based on a few number of data on earthquakes with $M_W \geq 8.0$, our estimate is between curves corresponding to relations from [*Wells and Coppersmith*, 1994] (obtained for thrusts) and [*Leonard*, 2010] or [*Thingbaijam et al.*, 2017] which are constructed from similar data (interplate or subduction dip-slip events) and very close to each other (Figure 7a). Taking into account that our moment magnitude can be underestimated due to a limited analyzed period range (Table 1), we can also consider for this event a moment magnitude of 8.8, determined in a wider period range in USGS (https://earthquake.usgs.gov/earthquakes/eventpage/us6000qw60/moment-tensor) (pale star in Figure 7a). In this case, the rupture length is closer to the relations by [*Leonard*, 2010] and [*Thingbaijam et al.*, 2017], and it is shorter and longer than lengths supposed in [*Wells and Coppersmith*, 1994] and [*Zavyalov and Zotov*, 2021], respectively. It should be mentioned that the July 29, 2025 mainshock is similar in its rupture length to the February 27, 2010 Maule earthquake (https://earthquake.usgs.gov/earthquakes/eventpage/official20100227063411530_30/finite-fault) and November 4, 1952 Kamchatka event according to its parameters reported by [*Johnson and Satake*, 1999] (Figure 7a). We can also see in Figure 7a that the scaling relations, constructed for interplate or subduction dip-slip events in [*Leonard*, 2010] or [*Thingbaijam et al.*, 2017], provide the best approximation for the results of this study, data from [*Johnson and Satake*, 1999], and the USGS finite-fault models available for earthquakes with $M_W \geq 8.0$ (except for the December 26, 2004 Sumatra-Andaman earthquake with $M_W = 9.1$ characterized by an extremely long rupture). Therefore, they should be preferred, for instance, for estimating moment magnitudes of paleoearthquakes (with corrections to surface rupture length) whose seismodislocations are as long as several hundreds of kilometers. As far as the largest foreshock and the September 13, 2025 aftershock are concerned, their rupture lengths are significantly longer than those imposed from all the discussed scaling relations while the rupture length of the September 18, 2025 aftershock is, similar to the mainshock, located between curves from [*Wells and Coppersmith*, 1994] (thrusts) and [*Leonard*, 2010] or [*Thingbaijam et al.*, 2017] (Figure 7b).

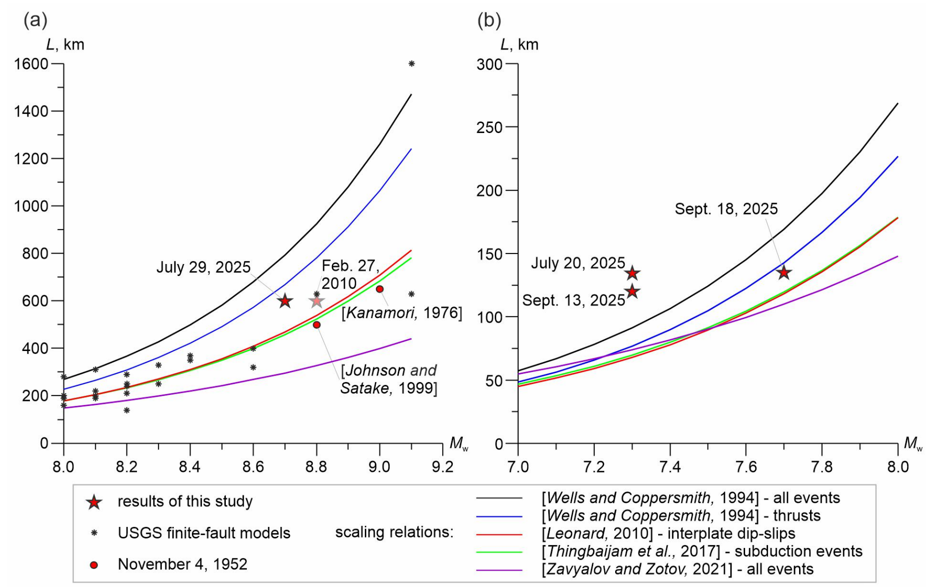

Figure 7. Rupture lengths, obtained in this study for the strong Kamchatka earthquakes in 2025, in comparison with some existing scaling relations in moment magnitude ranges of 8.0–9.1 (a) and 7.0–8.0 (b). Pale star in panel (a) marks our rupture length for the July 29, 2025 mainshock corresponding to moment magnitude of 8.8 determined in USGS. All the available rupture lengths from finite-fault USGS models for earthquakes with $M_W \geq 8.0$ are shown in panel (a).

4. Conclusion

We consider four strong earthquakes ($M_W > 7.0$) that occurred in 2025 near the Kamchatka Peninsula: the foreshock on July 20, mainshock on July 29, and two aftershocks on September 13 and 18. Their source parameters are estimated from teleseismic surface wave records in instant point and finite-fault (a shear elliptical dislocation with a finite duration) source approximations. The obtained results are analyzed in a framework of currently available USGS finite-fault models, source parameters of the November 4, 1952 Kamchatka earthquake, and some existing scaling relations between subsurface rupture length and magnitude. The following conclusions can be drawn.

1. The focal mechanisms, obtained for all the study earthquakes, are very similar to each other – they are pure or almost pure thrusts formed under the influence of the near horizontal SE-NW compression. This agrees well with the direction of the Pacific Plate subduction, an average focal mechanism for this segment of the Kuril-Kamchatka trench, and a regional strain field.
2. Proximity of focal mechanisms, determined by different authors and based on initial data in various period ranges, evidences for high percentage of double-couple component in the earthquake sources. This supports a statistical pattern showing that subduction thrust earthquakes are characterized by decreased non-double-couple component relative to strike-slips and normal faults due to larger and more uniform active tectonic settings.
3. Gently-dipping NE-SW nodal planes (with dip angles of 15–30°) are discriminated as the rupture (or fault) planes from surface wave analysis.
4. The obtained rupture lengths for the July 29, September 13 and 18, 2025 earthquakes are in agreement with the USGS finite-fault models while significantly longer rupture is determined in our study for the July 20, 2025 foreshock. Nevertheless, a spatial distribution of its aftershocks confirms our estimate of the rupture length.
5. The rupture lengths of the July 20, 2025 foreshock and September 13, 2025 aftershock are significantly longer than those imposed from all the discussed scaling relations. The rupture lengths of the July 29, 2025 mainshock and the September 18, 2025 aftershock are located between curves corresponding to the scaling relations from [*Wells and Coppersmith*, 1994] (thrusts) and [*Leonard*, 2010] or [*Thingbaijam et al.*, 2017]. Based on the additional data on the November 4, 1952 Kamchatka earthquake and all the available USGS finite-fault models for earthquakes with $M_W \geq 8.0$, the last two relations can be considered as the most preferred ones, for instance, for estimating moment magnitudes of paleoearthquakes (with corrections to surface rupture length) for which seismodislocations are as long as several hundreds of kilometers.

Acknowledgments. The study was carried out under the State Assignments of the affiliated organizations.

References

Bird P. An updated digital model of plate boundaries // Geochemistry, Geophysics, Geosystems. — 2003. — Vol. 4, no. 3. — P. 1027. — https://doi.org/10.1029/2001gc000252

Bukchin B. Determination of stress glut moments of total degree 2 from teleseismic surface wave amplitude spectra // Tectonophysics. — 1995. — Vol. 248, no. 3/4. — P. 185–191. — https://doi.org/10.1016/0040-1951(94)00271-a

Bukchin B. G. Determination of source parameters from surface wave recording allowing for uncertainties in the properties of medium // Izvestiya of the Academy of Sciences of the USSR. Physics of the Solid Earth. — 1990. — Vol. 25. — P. 723–728.

Bukchin B. G. Second-moment approximation of the earthquake source and fault plane identification // Izvestiya, Physics of the Solid Earth. — 2017. — Vol. 53, no. 2. — P. 243–249. — https://doi.org/10.1134/s1069351317020045

Bukchin B. G., Egorkin A. A. and Mostinskiy A. Z. Software complex FMT package. — 2005.

Bukchin B. G., Fomochkina A. S., Kossobokov V. G., et al. Characterizing the Foreshock, Main Shock, and Aftershock Sequences of the Recent Major Earthquakes in Southern Alaska, 2016-2018 // Frontiers in Earth Science. — 2020. — Vol. 8. — https://doi.org/10.3389/feart.2020.584659

DeMets C., Gordon R. G., Argus D. F., et al. Current plate motions // Geophysical Journal International. — 1990. — Vol. 101, no. 2. — P. 425–478. — https://doi.org/10.1111/j.1365-246x.1990.tb06579.x
Dziewonski A. M. and Anderson D. L. Preliminary reference Earth model // Physics of the Earth and Planetary Interiors. — 1981. — Vol. 25, no. 4. — P. 297–356. — https://doi.org/10.1016/0031-9201(81)90046-7
Dziewonski A. M. and Woodhouse J. H. An experiment in systematic study of global seismicity: Centroid-moment tensor solutions for 201 moderate and large earthquakes of 1981 // Journal of Geophysical Research: Solid Earth. — 1983. — Vol. 88, B4. — P. 3247–3271. — https://doi.org/10.1029/jb088ib04p03247
Filippova A., Fomochkina A., Kossobokov V., et al. Characterizing the foreshock, main shock, and aftershock sequences of the recent major earthquakes in Southern Alaska, 2020-2024 // Frontiers in Earth Science. — 2025. — Vol. 13. — https://doi.org/10.3389/feart.2025.1660221
Filippova A. I., Bukchin B. G., Fomochkina A. S., et al. Source process of the September 21, 2020 Mw 5.6 Bystraya earthquake at the South-Eastern segment of the Main Sayan fault (Eastern Siberia, Russia) // Tectonophysics. — 2022. — Vol. 822. — P. 229162. — https://doi.org/10.1016/j.tecto.2021.229162
Filippova A. I., Fomochkina A. S., Gileva N. A., et al. The September 6, 2021 MW 5.4 Tofalaria earthquake at a weakly active segment of the Main Sayan fault (Eastern Siberia) // Journal of Structural Geology. — 2024. — Vol. 188. — P. 105255. — https://doi.org/10.1016/j.jsg.2024.105255
Gorbatov A., Kostoglodov V., Suárez G., et al. Seismicity and structure of the Kamchatka Subduction Zone // Journal of Geophysical Research: Solid Earth. — 1997. — Vol. 102, B8. — P. 17883–17898. — https://doi.org/10.1029/96jb03491
Hanks T. and Kanamori H. A moment magnitude scale // Journal of Geophysical Research: Solid Earth. — 1979. — Vol. 84, B5. — P. 2348–2350. — https://doi.org/10.1029/jb084ib05p02348
Hayes G. P., Moore G. L., Portner D. E., et al. Slab2, a comprehensive subduction zone geometry model // Science. — 2018. — Vol. 362, no. 6410. — P. 58–61. — https://doi.org/10.1126/science.aat4723
Hayes G. P., Rivera L. and Kanamori H. Source Inversion of the W-Phase: Real-time Implementation and Extension to Low Magnitudes // Seismological Research Letters. — 2009. — Vol. 80, no. 5. — P. 817–822. — https://doi.org/10.1785/gssrl.80.5.817
Heidbach O., Rajabi M., Reiter K., et al. World stress map 2016. — GFZ Data Service, 2016. — https://doi.org/10.5880/WSM.2016.002
Ji C., Wald D. J. and Helmberger D. V. Source Description of the 1999 Hector Mine, California, Earthquake, Part I: Wavelet Domain Inversion Theory and Resolution Analysis // Bulletin of the Seismological Society of America. — 2002. — Vol. 92, no. 4. — P. 1192–1207. — https://doi.org/10.1785/0120000916
Johnson J. M. and Satake K. Asperity Distribution of the 1952 Great Kamchatka Earthquake and its Relation to Future Earthquake Potential in Kamchatka // Pure and Applied Geophysics. — 1999. — Vol. 154, no. 3/4. — P. 541–553. — https://doi.org/10.1007/s000240050243
Kagan Y. Y. 3-D rotation of double-couple earthquake sources // Geophysical Journal International. — 1991. — Vol. 106, no. 3. — P. 709–716. — https://doi.org/10.1111/j.1365-246X.1991.tb06343.x
Kagan Y. Y. Simplified algorithms for calculating double-couple rotation // Geophysical Journal International. — 2007. — Vol. 171, no. 1. — P. 411–418. — https://doi.org/10.1111/j.1365-246X.2007.03538.x
Kanamori H. Re-examination of the earth's free oscillations excited by the Kamchatka earthquake of November 4, 1952 // Physics of the Earth and Planetary Interiors. — 1976. — Vol. 11, no. 3. — P. 216–226. — https://doi.org/10.1016/0031-9201(76)90066-2
Kanamori H. and Rivera L. Source inversion of W phase: speeding up seismic tsunami warning // Geophysical Journal International. — 2008. — Vol. 175, no. 1. — P. 222–238. — https://doi.org/10.1111/j.1365-246x.2008.03887.x
Keilis-Borok V. I. Recording, Identification, and Measurement of Surface Wave Parameters // Seismic Surface Waves in a Laterally Inhomogeneous Earth / ed. by V. I. Keilis-Borok. — 1989. — P. 131–182. — https://doi.org/10.1007/978-94-009-0883-3_5
Kogan M. G., Frolov D. I., Vasilenko N. F., et al. Plate coupling and strain in the far western Aleutian arc modeled from GPS data // Geophysical Research Letters. — 2017. — Vol. 44, no. 7. — P. 3176–3183. — https://doi.org/10.1002/2017gl072735
Lasserre C., Bukchin B., Bernard P., et al. Source parameters and tectonic origin of the 1996 June 1 Tianzhu (Mw=5.2) and 1995 July 21 Yongden (Mw=5.6) earthquakes near the Haiyuan fault (Gansu, China) // Geophysical Journal International. — 2001. — Vol. 144, no. 1. — P. 206–220. — https://doi.org/10.1046/j.1365-246x.2001.00313.x
Leonard M. Earthquake Fault Scaling: Self-Consistent Relating of Rupture Length, Width, Average Displacement, and Moment Release // Bulletin of the Seismological Society of America. — 2010. — Vol. 100, 5A. — P. 1971–1988. — https://doi.org/10.1785/0120090189

Melnikova V. I. Crustal strain parameters in the Baikal Rift Zone from seismic data : PhD thesis / Melnikova V. I. — Irkutsk, 2008. — (In Russian).

Mendiguren J. A. Inversion of surface wave data in source mechanism studies // Journal of Geophysical Research. — 1977. — Vol. 82, no. 5. — P. 889–894. — https://doi.org/10.1029/jb082i005p00889

Nataf H.-C. and Ricard Y. 3SMAC: an a priori tomographic model of the upper mantle based on geophysical modeling // Physics of the Earth and Planetary Interiors. — 1996. — Vol. 95, no. 1/2. — P. 101–122. — https://doi.org/10.1016/0031-9201(95)03105-7

Nishizawa T., Nakamura H., Churikova T., et al. Genesis of ultra-high-Ni olivine in high-Mg andesite lava triggered by seamount subduction // Scientific Reports. — 2017. — Vol. 7, no. 1. — https://doi.org/10.1038/s41598-017-10276-3

Rösler B. and Stein S. Consistency of Non-Double-Couple Components of Seismic Moment Tensors with Earthquake Magnitude and Mechanism // Seismological Research Letters. — 2022. — Vol. 93, no. 3. — P. 1510–1523. — https://doi.org/10.1785/0220210188

Ruppert N. A., Lees J. M. and Kozyreva N. P. Seismicity, earthquakes and structure along the Alaska-Aleutian and Kamchatka-Kurile Subduction Zones: A review // Volcanism and Subduction: The Kamchatka Region. — American Geophysical Union, 2007. — P. 129–144. — https://doi.org/10.1029/172gm12

Seredkina A. I., Melnikova V. I., Radziminovich Y. B., et al. Seismicity of the Erguna Region (Northeastern China): Evidence for Local Stress Redistribution // Bulletin of the Seismological Society of America. — 2020. — Vol. 110, no. 2. — P. 803–815. — https://doi.org/10.1785/0120190182

Sipkin S. Estimation of earthquake source parameters by the inversion of waveform data: synthetic waveforms // Physics of the Earth and Planetary Interiors. — 1982. — Vol. 30, no. 2/3. — P. 242–259. — https://doi.org/10.1016/0031-9201(82)90111-x

Thingbaijam K. K. S., Martin Mai P. and Goda K. New Empirical Earthquake Source-Scaling Laws // Bulletin of the Seismological Society of America. — 2017. — Vol. 107, no. 5. — P. 2225–2246. — https://doi.org/10.1785/0120170017

Wells D. L. and Coppersmith K. J. New empirical relationships among magnitude, rupture length, rupture width, rupture area, and surface displacement // Bulletin of the Seismological Society of America. — 1994. — Vol. 84, no. 4. — P. 974–1002. — https://doi.org/10.1785/bssa0840040974

Xu D., Wang W. and Ren Z. Preliminary slip distribution of the July 29, 2025 M 8.8 Kamchatka, Russia earthquake // Earthquake Research Advances. — 2025. — P. 100427. — https://doi.org/10.1016/j.eqrea.2025.100427

Zaccagnino D. and Doglioni C. The impact of faulting complexity and type on earthquake rupture dynamics // Communications Earth & Environment. — 2022. — Vol. 3, no. 1. — https://doi.org/10.1038/s43247-022-00593-5

Zavyalov A. D. and Zotov O. D. A New Way to Determine the Characteristic Size of the Source Zone // Journal of Volcanology and Seismology. — 2021. — Vol. 15, no. 1. — P. 19–25. — https://doi.org/10.1134/s0742046321010139